HHS Public Access

Author manuscript

Ann Biomed Eng. Author manuscript; available in PMC 2023 April 01.

Published in final edited form as:

Ann Biomed Eng. 2023 April ; 51(4): 846–863. doi:10.1007/s10439-022-03102-z.

Contractile Adaptation of the Left Ventricle Post-myocardial Infarction: Predictions by Rodent-Specific Computational Modeling

Emilio A. Mendiola[1], **Sunder Neelakantan**[1], **Qian Xiang**[2], **Samer Merchant**[3], **Ke Li**[2], **Edward W. Hsu**[3], **Richard A. F. Dixon**[2], **Peter Vanderslice**[2], **Reza Avazmohammadi**[1,4,5]

[1]Computational Cardiovascular Bioengineering Laboratory, Department of Biomedical Engineering, Texas A&M University, College Station, TX, USA

[2]Department of Molecular Cardiology, Texas Heart Institute, Houston, TX, USA

[3]Department of Biomedical Engineering, University of Utah, Salt Lake City, UT, USA

[4]J. Mike Walker ’66 Department of Mechanical Engineering, Texas A&M University, College Station, TX, USA

[5]Department of Cardiovascular Sciences, Houston Methodist Academic Institute, Houston, TX, USA

Abstract

Myocardial infarction (MI) results in cardiac myocyte death and the formation of a fibrotic scar in the left ventricular free wall (LVFW). Following an acute MI, LVFW remodeling takes place consisting of several alterations in the structure and properties of cellular and extracellular components with a heterogeneous pattern across the LVFW. The normal function of the heart is strongly influenced by the passive and active biomechanical behavior of the LVFW, and progressive myocardial structural remodeling can have a detrimental effect on both diastolic and systolic functions of the LV leading to heart failure. Despite important advances in understanding LVFW passive remodeling in the setting of MI, heterogeneous remodeling in the LVFW *active* properties and its relationship to organ-level LV function remain understudied. To address these gaps, we developed high-fidelity finite-element (FE) rodent computational cardiac models (RCCMs) of MI using extensive datasets from MI rat hearts representing the heart remodeling from one-week (1-wk) to four-week (4-wk) post-MI timepoints. The rat-specific models (n = 2 for each timepoint) integrate detailed imaging data of the heart geometry, myocardial fiber architecture, and infarct zone determined using late gadolinium enhancement prior to terminal measurements. The computational models predicted a significantly higher level of active tension in remote myocardium in early post-MI hearts (1-wk post-MI) followed by a return to near the control level in late-stage MI (3- and 4-wk post-MI). The late-stage MI rats showed smaller

Address correspondence to Reza Avazmohammadi, Computational Cardiovascular Bioengineering Laboratory, Department of Biomedical Engineering, Texas A&M University, College Station, TX, USA. rezaavaz@tamu.edu.

COMPETING INTERESTS The authors declare no conflict of interest.

SUPPLEMENTARY INFORMATION

The online version contains supplementary material available at https://doi.org/10.1007/s10439-022-03102-z.

myofiber ranges in the remote region and *in-silico* experiments using RCCMs suggested that the smaller fiber helicity is consistent with lower contractile forces needed to meet the measured ejection fractions in late-stage MI. In contrast, *in-silico* experiments predicted that collagen fiber transmural orientation in the infarct region has little influence on organ-level function. In addition, our MI RCCMs indicated that reduced and potentially positive circumferential strains in the infarct region at end-systole can be used to infer information about the time-varying properties of the infarct region. The detailed description of regional passive and active remodeling patterns can complement and enhance the traditional measures of LV anatomy and function that often lead to a gross and limited assessment of cardiac performance. The translation and implementation of our model in patient-specific organ-level simulations offer to advance the investigation of individualized prognosis and intervention for MI.

Keywords

Myocardial infarction; Cardiac biomechanics; Remodeling; Computational modeling

INTRODUCTION

Myocardial infarction (MI) results in cardiomyocyte death and the formation of a fibrotic scar in the left ventricle (LV). After an acute MI, the LV undergoes a cascade of remodeling events at various length scales in an attempt to cope with the absence of contractility and increased stiffness in the scar region.[36,43,47] Infarcted myocardium undergoes a healing process including four phases: (i) acute ischemia, (ii) necrosis, (iii) fibrosis, and (iv) remodeling, through which the structure and mechanical properties of the scar region are expected to be altered.[21] In addition to alterations in the scar region, the remaining remote myocardium may undergo continual changes in contractility and architecture in an attempt to compensate for the loss of contractile ability of the infarct. Such adaptations that remain understudied could occur immediately post-MI and continue for several months. Also, although global metrics of LV pump function are important in inferring post-MI remodeling, they are limited indications of the state of the remodeling process at the tissue level with inadequate predictive capability.[26,50] Advancing the knowledge of the relationship between chronic tissue-level remodeling events and LV functional adaptations post-MI will improve the ability to stratify MI patients based on the risk of future poor outcomes and plan individualized therapies.

The structure of the myocardium heavily influences the biomechanical behavior of the LVFW and, thus, determines the contractile patterns of the LV.[8,13] Multiple multiscale remodeling events, triggered at different times during scar maturation and occurring at different rates, contribute to net changes in tissue stiffness and anisotropic behavior. Soon after MI, collagen fibers begin to be deposited in the scar region. At later timepoints, myofibers may show increased stiffness and undergo changes in orientation. These changes ultimately drive organ-level anatomical changes, including LV dilation and wall thinning. While the time-course structural and mechanical changes of the scar region have been studied previously, identifying and studying the isolated effect of individual passive and active remodeling mechanisms on tissue biomechanics and LV function post-MI will assist

with understanding adaptive vs. maladaptive nature of these remodeling events and the extent to which these events contribute to LV dysfunction post-MI.

Despite strong evidence supporting the importance of myocardial mechanics in remodeling post-MI,[45,49] the assessment of temporal regional LV contractile forces proves to be challenging. The majority of *in-vivo* MI studies rely on global metrics of LV function, such as ejection fraction (EF) and global longitudinal strain (GLS). While these metrics are useful in characterizing organ-level function, they fall short of capturing regional adaptations in contractility. Also, although myocardial strains have been successfully explored as a measure of function and predictor of outcomes in structural heart disease,[46] they provide a confounded picture of contractility as strains are driven by both passive stiffness and active contraction. In contrast, image-based inverse modeling bridging between tissue-level properties to organ-level function holds promise to estimate contractile properties, provide insights into the mechanisms of remodeling, and serve as an early patient-specific prognostic tool. In acute MI, the infarct region loses its contractile ability and begins to stiffen. Dynamic remodeling events in the healing scar region contribute to heterogeneous stiffening, and a reduction of circumferential and longitudinal strains as the myocardium converts from an active state to solely passive behavior. The coupling between the remote myocardium and infarcted tissue and remodeling of the remote myocardium contribute to alterations of the contractile pattern of the remaining remote myocardium.[7] The contractile adaptation of the remote myocardium may serve as a major determinant of long-term functional outcomes and is influenced by remodeling in the scar region. We hypothesize that the characterization of the time-course remodeling of both the infarct and remote regions post-MI will improve our understanding of the competition between passive and active remodeling events in the LVFW and their contribution to changes in the LV contractile function.

In the present study, we developed subject-specific rodent computational cardiac models (RCCMs) using extensive data sets from rat hearts with anterior MI representing the remodeling stages from 1- to 4-week post-MI. Our pipeline integrates image-based characterizations of the heterogeneous remodeling of LVFW active biomechanics with *ex-vivo* mechanical testing data and allowed us to study the isolated effect of remodeling events on organ-level function as MI proceeds from early-stage-scarring to late-stage remodeling. We used the model to predict changes in contractile forces post-MI at multiple timepoints while accounting for changes in the LV anatomy and hemodynamics, LVFW architecture, and infarct properties in an animal-specific manner. We further used our RCCMs to investigate relations between changes in regional strains and passive and active myocardial remodeling post-MI, and study the effect of architectural remodeling in the scar on strain distribution and LV function. Findings from our preliminary study improve our understanding of potential active remodeling in the LVFW post-MI and serve as an essential step in identifying tissue-level remodeling-based markers, incremental to organ-level performance metrics. Such markers will facilitate the use of remodeling patterns to enhance the traditional measures of LV function that often lead to gross and limited information on cardiac performance. Ultimately, the development and implementation of our RCCM in patient-specific organ-level simulations will allow for individualized prognosis and intervention for MI.

MATERIALS AND METHODS

We developed subject-specific finite-element (FE) RCCMs of MI using extensive datasets, incorporating *ex-vivo* and *in-vivo* experimental measurements, from normal and post-MI rat hearts at four timepoints (Fig. 1). The details of the measurements and modeling are given below.

Rodent Model of MI

All animals used in this work were treated in accordance with guidelines approved by the Institutional Animal Care and Use Committee (IACUC) at the Texas Heart Institute, and all procedures were performed following protocols approved by the Texas Heart Institute's IACUC. A total of ten male Wistar–Kyoto (WKY) rats, 8 weeks old at the start of the experiment, were used in this study. Anteriobasal infarct was induced in eight rats by ligation of the left anterior descending artery near the base of the heart. Animals were sacrificed at 1-, 2-, 3-, and 4-week post-MI timepoints (hereafter referred to as 1-, 2-, 3-, and 4-wk, respectively). Two animals were used as control subjects and were sacrificed one week after receiving sham surgery. The ten subjects ($n = 2$ at each timepoint) were used to develop subject-specific FE RCCMs.

Hemodynamic Measurements and Heart Preparation

Prior to sacrifice, pressure–volume (P–V) measurements of the LV were collected. Subjects in the infarct groups were then given gadolinium contrast agent, branded as Gado-DTPA*rmTM* (0.5 mmol gadopentetate dimeglumine/mL, BioPAL, Inc.) in the tail vein at 0.4 μL/g and allowed to circulate for 20 min for magnetic resonance imaging (MRI) enhancement. Control animals received a similar injection of buffered saline. Next, 0.2 mL heparin was injected *via* the superior vena cava and allowed to circulate for 3 min. After sacrifice and excision, blood was flushed out from the heart using phosphate-buffered saline. Two catheters, inserted into aortic and pulmonary arteries, were used to infuse octreotide solution to close the mitral and tricuspid valves and maintain the internal geometry of both ventricles at about the end-diastolic (ED) pressure. Heart tissues were immediately put in a 10% formalin solution for fixation. Imaging was conducted with the hearts in the approximate ED configuration.

Geometry and Fiber Architecture Acquisition

High-resolution cardiac MRI scans were performed on the prepared hearts using a Bruker Biospec 7T (Billerica, MA) scanner. Late-gadolinium enhancement (LGE) scans followed by diffusion tensor imaging (DTI) were performed at the same configuration for each heart. Myofiber and sheet orientations were determined after post-processing the local diffusion tensors obtained from the DTI data. Infarct volume, as a percent of LVFW volume, was calculated from LGE imaging. All the scans were performed at an isotropic 100 μm resolution (FOV 17.5 × 22.5 × 5 mm, TR = 500 ms, and TE = 23 ms) over a period of 12 h. The DTI accuracy was 5°. Further specifics of the scan sequence are provided in Ref. [4].

MI Rodent Computational Cardiac Model Development

The development of the rat-specific FE RCCMs consisted of five main steps: (i) reconstruction and meshing of the biventricular geometry, (ii) determination and assignment of the remote and infarct regions, (iii) registration of the myofiber orientation to the meshed geometry, (iv) incorporation of the passive and active constitutive laws, and (v) completion of an inverse problem to estimate contractile tension. Two heart models were developed at each timepoint.

Identification of Remote and Infarct Regions

The segmentation and reconstruction of the 3-D full heart geometry from MRI scans were performed using Mimics (Materialise, Leuven, Belgium). The geometries for both control and post-MI hearts were truncated below the valve plane and meshed using quadratic tetrahedral elements (Fig. 2). The remote and infarct regions of the post-MI heart models were determined in several steps. First, the infarct region was determined by identifying areas of the LGE MRI that showed increased contrast relative to remote myocardium.[37] The infarct region was also evident in DTI scans as a region with no signal or disturbed fibers. The geometric dimensions of the infarct regions developed from LGE T1 scans were consistent with the regions seen in DTI scans. The remaining regions in the reconstructed heart (including right ventricular and septal regions) were considered to belong to the remote region.

Regional Fiber Architecture in Remote and Infarct Regions

The myofiber orientation distribution in the remote region, reconstructed from DTI scans and weighted by principal directions at each voxel, was registered to the corresponding ventricular mesh from the same rodent heart. As the number of voxels was much higher than that of elements,[4,28] a single preferred (fiber) direction for each element centroid was estimated by taking a weighted average of all the directions contained within a spherical neighborhood of each element centroid.[4] The infarct region is characterized by the loss of myofibers and deposition of collagen fibers. Previous investigations have found that newly deposited collagen fibers are highly aligned within each transmural layer.[22] Additionally, both increased alignment of collagen fibers and maintenance of the organized counterclockwise rotation from epicardium to endocardium, which could be statistically represented by average myofiber orientation in the remote LVFW regions, has been observed in the infarct scar.[2,54] In this study, we calculated the average fiber direction in three manually defined transmural regions of the remote LVFW tissue: endocardium, midwall, and epicardium. The fiber direction of mesh elements in each transmural layer within the infarct was assigned to be the same as the average directions in the respective depth in the remote region.

Material Model for the Myocardium

The myocardium was modeled as a transversely isotropic hyperelastic material characterized by one fiber direction. A constitutive model based on additive stress decomposition for passive and active behaviors[3] was used in the form of

$$\mathbf{T} = \underbrace{\frac{1}{J}\overline{\mathbf{F}}\frac{\partial W^{\text{dev}}}{\partial \overline{\mathbf{E}}}\overline{\mathbf{F}}^{T} + \frac{\partial W^{\text{vol}}}{\partial J}}_{\text{Passive}} + \underbrace{\frac{1}{J}\mathbf{F}\mathbf{S}^{\text{act}}\mathbf{F}^{T}}_{\text{Active}}, \tag{1}$$

where $\mathbf{T}$ is the total Cauchy stress, $\mathbf{F}$ is the deformation gradient, J denotes the deformation volumetric changes, and $\overline{\mathbf{F}} = J^{-1/3}\mathbf{F}$ is the deviatoric part of $\mathbf{F}$. The passive stress was described using a Fung-type strain energy function[20] given by

$$W(\mathbf{E}, J) = \underbrace{c[\exp(Q(\mathbf{E})) - 1]}_{W^{\text{dev}}} + \underbrace{\frac{K}{2}\left[\frac{J^2 - 1}{2} - \ln(J)\right]}_{W^{\text{vol}}}, \tag{2}$$

where W^{dev} and W^{vol} denote the deviatoric and volumetric components, respectively, and $\mathbf{E}$ is the Green-Lagrange strain tensor. The quadratic form Q is expressed as

$$Q = B_1\overline{E}_{11}^2 + B_2(\overline{E}_{22}^2 + \overline{E}_{33}^2 + \overline{E}_{23}^2) + B_3(\overline{E}_{12}^2 + \overline{E}_{13}^2), \tag{3}$$

where $\overline{\mathbf{E}} = (\overline{\mathbf{F}}^{T}\overline{\mathbf{F}} - \mathbf{I})/2$ and the Cartesian coordinate system $\{\mathbf{e}_1, \mathbf{e}_2, \mathbf{e}_3\}$ denotes the local preferred material directions with the fiber direction being along $\mathbf{e}_1$. In these equations, c is a positive stress-like constant, B_1, B_2, and B_3 are dimensionless constants characterizing the local anisotropy in the myocardium, and K is the bulk modulus.

A constitutive equation for the active stress can be written in terms of the second Piola–Kirchhoff active stress tensor as

$$\mathbf{S}^{\text{act}} = \frac{T_a(E_f)}{2E_f + 1}\mathbf{N} \otimes \mathbf{N}, \tag{4}$$

where $T_a(E_f)$ is a stress-like positive function of the strain in the fiber direction $\mathbf{N}$ given by $E_f = \mathbf{N} \cdot \mathbf{E}\mathbf{N}$. We chose the following form for $T_a(E_f)$

$$T_a(E_f) = T_{\text{Ca}^{2+}}\left[1 + \beta\left(\sqrt{2E_f + 1} - 1\right)\right], \tag{5}$$

following the Hunter–McCulloch–TerKeurs model[24] for the mechanical behavior of a contractile myocyte. In this model, the active force $T_{\text{Ca}^{2+}}$, generated for resting myofibers, increases by a positive factor β when myofibers are extended to the strain E_f, obeying the Frank–Starling relationship.[19] In addition, we made the simplifying assumption that the activation spatial pattern is homogeneous within each region of the biventricular model. Finally, the incompressibility constraint was enforced in the passive part by setting the bulk modulus $K >> c$ in the penalty term (Eq. 2).

Passive Parameter Estimation

Hearts used for DTI and subject-specific organ-level modeling were not usable for histology or passive biaxial testing. To estimate the passive parameters, we made use of mean stress–strain curves obtained from biaxial testing of a similar cohort (six hearts per timepoint; same rodent strain, sex, and age) taken from a parallel study.[40] An inverse problem approach was

used to estimate the phenomenological-type passive material properties of the remote and infarct region for each timepoint.

Briefly, thirty hearts ($n = 6$ per timepoint) were used for biaxial mechanical testing. Full-thickness rectangular specimens of the full LVFW (including both infarct and remote regions post-MI) were isolated from the hearts, with the slab edges being aligned with the longitudinal, circumferential, and radial directions of the LV. Specimens were mounted in a biaxial mechanical testing machine (Cellscale Biotester, CellScale, Waterloo). Mechanical testing consisted of 10 cycles of preconditioning, followed by an equibiaxial displacement-controlled loading protocol. The stretching protocol was applied as a cyclic deformation with a rate of 1% stretch per second to minimize inelastic effects. The LVFW specimens were partially submerged in phosphate-buffered saline at 20 °C during the tests to prevent dehydration. Individual stressstrain curves at each timepoint were averaged to produce a mean curve for each timepoint. Subsequently, specimens were fixed in 10% formalin to preserve the fibrous architecture for histological studies. The specimens were sectioned transmurally across the LVFW thickness resulting in a total of ~10 sections per specimen, each 5 μm thick. Sections were then stained using Picrosirius red to characterize the transmural myo- and collagen fiber architecture. Two-dimensional images acquired from stained sections were processed *via* custom image-processing in-house algorithms to characterize the myofiber structure and quantify the volume fraction of each fiber component (Fig. S1).

We defined the total energy function characterizing the passive behavior of the LVFW specimens as the sum of remote and infarct energies given by:

$$W^{\text{total}} = \phi^r W^r + \phi^i W^i, \quad r: \text{remote}, \quad i: \text{infarct}, \tag{6}$$

where ϕ^r and ϕ^i are the mean remote and infarct volume fractions, respectively, over the entire LVFW calculated from histology, and W^r and W^i describe the Fung-type exponential energy function (Eq. 2) corresponding to the remote and infarct contributions to the total strain energy W^{total}, respectively. While the phenomenological material model 2 does not explicitly separate the contributions of myofibers and collagen fibers to the energy function (in contrast to structurally based models[6]), W^r and W^i portions in Eq. 6 are expected to primarily represent myofiber and collagen fiber contributions, respectively. Eight material parameters were estimated, denoted by $\{c^r, B_1^r, B_2^r, B_3^r\}$ and $\{c^i, B_1^i, B_2^i, B_3^i\}$. The constants c^r, B_1^r, B_2^r, and B_3^r for remote myocardium were obtained by assuming no contribution from the infarct region (setting $\phi^i = 0$) and performing an analytical fit of the constitutive model (Eq. 6) to biaxial data of the control group ($n = 6$). Using the parameter reformulation described by Xi *et al.*,[52] a bulk stiffness parameter was defined as $c \times a$ where

$$\alpha^s = B_1^s + B_2^s + B_3^s; \; s = r, \; i \, . \tag{7}$$

The mean passive parameters identified for the remote myocardium were kept constant in W^r and used as inputs for the infarct parameter estimation in all the post-MI timepoints, under the assumption that only the infarct region undergoes (passive) biomechanical alterations post-MI. The mean passive constants for the infarct timepoints were then

estimated by fitting the energy function (Eq. 6) with varying constants $\{c^i,\ B_1^i,\ B_2^i,\ B_3^i\}$ in W^i to match the results of the individual tissue-level stress-strain biaxial results from the corresponding timepoint.

In the organ-level RCCM, the estimated control passive parameters $\{c^r,\ B_1^r,\ B_2^r,\ B_3^r\}$ were applied to the control hearts and to the remote myocardium regions of the infarcted heart models, under the assumption that the remote myocardium properties are not altered post-MI. The mean passive parameters estimated for the infarct timepoints $\{c^i,\ B_1^i,\ B_2^i,\ B_3^i\}$ were applied only to the infarct region of the hearts (defined using LGE-MRI) from the same timepoint.

Active Parameter Estimation

Once passive properties for the remote and infarct regions were estimated from biaxial tests results, organ-level inverse simulations were used to estimate the active tension $T_{Ca^{2+}}$ by reproducing the animal-specific P–V loop measurements using inverse modeling.[4] Briefly, an inverse minimization problem was conducted in which a discretized pressure wave (measured by LV catheterization) was applied to the *in-silico* biventricular model as input, and a guess for the active parameter $T_{Ca^{2+}}$ was made. An error was calculated as the squared difference between the measured ventricular volume and the simulated volume. The minimization algorithm was iteratively conducted to minimize this error. $T_{Ca^{2+}}$ was estimated once error fell below a specified threshold (0.1 μL).

The remaining parameter present in the active model, β, modulates the fiber length dependency. While fiber length-dependency coefficient remains constant in all the MI models ($\beta = 1.4$), changes in preload are accounted for by (i) using animal-specific geometry entailing LV eccentric hypertrophy, and (ii) estimating the reference configuration for each MI heart using the animal-specific ED configuration as input. Once the reference configuration is estimated, the initial loading from the reference to ED configuration produces the animal-specific regional preload prior to the activation. The reference configuration was estimated by unloading the heart models, reconstructed at the ED configuration, to zero pressure. We considered this unloaded state to be stress-free reference configuration. The active inverse problem was conducted once both ventricles were pressurized to their ED pressures. Experimentally-measured pressure (over the entire cardiac cycle) was applied and $T_{Ca^{2+}}$ was estimated as previously described.

In-Silico Experiments: Altered Regional Fiber Architecture

The RCCMs of MI developed here were well-suited for *in-silico* investigation of structure-function relationship post-MI.[29] We conducted numerical experiments to study the independent effect of fiber architecture in the remote and infarct zones on organ-level LV function. The first set of experiments investigated the effect of remote myocardium fiber range on LV contractility. Two synthetic fiber architectures with varying fiber ranges were developed for the 3-wk (Subject 1) and 4-wk (Subject 1) heart models. An inverse problem to estimate the active force parameter $T_{Ca^{2+}}$ was conducted with each synthetic fiber structure. The second set of experiments was intended to investigate the effect of infarct fiber architecture on organ-level function. In this experiment, the transmurally

varying infarct fiber structure, used in the animal-specific simulations, was replaced with a transmurally uniform architecture of a given fixed fiber direction. Forward simulations were conducted with prescribed fiber direction of 90°, 45°, and 0° in the infarct region at all post-MI timepoints.

Statistical Analysis

Estimated passive parameters are presented as means ± standard deviation. Anatomical, hemodynamic, and estimated active parameters are presented in tables as single values and in bar plots as mean ± standard deviation. Statistical analysis was accomplished by using one-way ANOVA followed by a Tukey post hoc test. A p value of < 0.05 was considered statistically significant. All tests were conducted using Prism 9 software (GraphPad Software, San Diego, CA).

RESULTS

Anatomical and Hemodynamic Adaptation

Various differences were observed in the LV function from control to post-MI. Characteristics of the P–V loop measurements for the animals at each timepoint post-MI are presented in Table 1 and Fig. S2. Mean EDV was increased compared to control at all timepoints, except 2-wk, with a nearly twofold increase (p ~0.7 for all timepoints). Subjects at the 2-wk timepoint indicated little change in EDV compared to the control. Stroke volume (SV) was slightly increased at the 1-wk timepoint compared to the control ($p = 0.83$), and was at near normal values in the late-stage post-MI animals (3- and 4-wk). EF was decreased compared to control at all post-MI timepoints, with the lowest EF observed in the 4-wk subjects (approximately 44% of the control value, $p = 0.35$).

End-systolic pressure (ESP) in the LV was higher than control post-MI with a maximum mean value at the 3-wk timepoint while end-diastole pressure (EDP) remained lower than that of the control post-MI. A decrease in Tau (relaxation time constant) was observed in early MI (1-wk, $p = 0.52$) suggesting impaired relaxation in the LV post-MI corroborated with corresponding (approximately 50%, $p = 0.93$) decrease in minimum dP/dt during isovolumetric relaxation. At later timepoints, Tau remained nearly at the level of the control subjects. Arterial elastance (Ea), a measure of arterial afterload, increased throughout the scar maturation process, peaking in the 4-wk subjects at a value greater than 300% of the control ($p = 0.27$).

Considerable LV wall thinning and significant infarct expansion were observed in the 3- and 4-wk timepoints (Fig. S3). The LVFW infarct region thickness decreased by ~ 34% on average at the 4-wk timepoint compared to the same subject's healthy thickness (Table 2). The infarct region was significantly larger at later timepoints (Fig. S3); observations indicated the infarct region made up approximately 10% of the volume of the LV chamber in the 1-wk subjects and 25% in the 4-wk subjects.

Passive Behavior Adaptations

Biaxial mechanical testing of full LVFW specimens (Fig. 3a) indicated the long-term post-MI tissues (4-wk timepoint) have a stiffer response in both circumferential and longitudinal (apex-to-base) directions (Figs. 3c, 3d), consistent with previous investigations.[1,35] A significantly larger increase in terminal stress from control to 4-wk cases was noted in the circumferential direction (Fig. S4, $p < 0.001$). Satisfactory goodness-of-fits were found for the passive fits to the mean non-linear stress-strain behavior of the control and infarcted LVFW specimens (estimated passive parameters are reported in Table 3 and a representative fit is displayed in Fig. 3e). The bulk stiffness parameter ($c \times a$, Table 3) was estimated regionally, providing a measure of the increased stiffness in the infarct region relative to the remote healthy tissue. Increases in the bulk stiffness of the infarct region indicated a significantly stiffer response at late post-MI timepoints (3- and 4-wk) compared to that of the control (Table 3, Fig. S4). DTI data indicated remarkable differences in the fiber architecture in the remote myocardium between control and post-MI timepoints (Table 2). DTI calculations indicated reduced transmural myofiber orientation range in the remote myocardium at post-MI timepoints. Fibers in the endocardium were more closely aligned with the circumferential direction (Table 3). Histology indicated the collagen fibers in the infarct region closely followed the fiber architecture of the myofibers (a representative quantification of the transmural LVFW fiber structure is displayed in Fig. 3b). A circumferential shift in the infarct collagen fibers is consistent with previously published data.[35]

Increased Contractility in Remote Myocardium

The RCCMs were used to estimate the adaptation of the active behavior in the remote myocardium post-MI using rat-specific P–V measurements (Fig. 4a). Our modeling framework allowed us to capture the full-cycle subject-specific active contraction parameter, $T_{Ca^{2+}}$ at each timepoint (Fig. 4b). The mean peak magnitude of $T_{Ca^{2+}}$ in the remote region increased significantly ($p < 0.01$, Fig. 5), to approximately 370% of the normal value, immediately post-MI in the 1-wk model (Table 4). $T_{Ca^{2+}}$ was slightly reduced at 2-wks compared to the 1-wk timepoint. At the 3- and 4-wk timepoints, contractility decreased significantly compared to the 1-wk post-MI timepoint ($p = 0.01$ and $p < 0.01$, respectively) to approximately normal values (Table 4, Fig. 5).

Cardiac Strain Adaptations

The magnitude of the predicted peak end-systolic strains (Table 5) for the control RCCMs were in agreement with previously reported strain measures (0.183 vs. 0.177 and 0.167 vs. 0.164 in the circumferential and longitudinal directions, respectively).[14] At early post-MI timepoints, both circumferential and longitudinal strains in the remote regions were reduced compared to those from the normal model (Table 5 and Fig. 7). Circumferential strains in the remote region were at nearly control values in the 2-wk RCCM, but deteriorated further in the late-stage post-MI models (3- and 4-wk). In the infarct region, both circumferential and longitudinal strains were reduced in late-stage MI (3- and 4-wk timepoints) (Fig. 6). Both strains reached their lowest absolute values at the final timepoint (4-wk), coinciding with the

timepoint at which biaxial experiments indicated the greatest passive stiffness. It was noted that the LVFW in 4-wk balloons outward, unlike at any other timepoints (Fig. 7).

Effect of Architecture on Cardiac Strain and Function

Inverse modeling with synthetic fiber architectures in remote myocardium (through which a new $T_{Ca^{2+}}$ was estimated) resulted in a decrease in the predicted active tension necessary to maintain a given EF as fiber range was reduced in both 3- and 4-wk heart models (Table 6). In contrast, only minor differences in LVEF was indicated by the forward simulations of the RCCMs at any timepoint when altering the fiber structure of the infarct region (Table 7). Positive circumferential strain in the infarct region increased as fibers move away from the circumferential direction (0°) towards the longitudinal direction (90°) (Fig. 8). Circumferential strain in the remote region was hardly affected in the 1-wk model, whereas positive circumferential strain increased in the remote myocardium of the 4-wk model as the synthetic fiber structure moved towards the longitudinal direction.

DISCUSSION

We have presented RCCMs that incorporate the passive remodeling events and functional adaptations that occur after acute MI to estimate potential active adaptations in the remote myocardium. To the best of our knowledge, RCCMs presented here are the first to integrate imaging and mechanical data to estimate the active contractility and contractile patterns of the LV in a cross-sectional cohort at different timepoints post-MI. The incorporation of architectural and mechanical adaptations occurring at fiber and tissue levels allowed us to link remodeling events with LV organ-level function at various stages in the infarct scar maturation process. Our modeling framework holds promise to predict the outcome of the complex interplay between various mechanical remodeling events in response to MI and enable the identification of key mechanisms at the fiber and tissue levels determining the LV function during the infarct healing process.

Anatomical and Hemodynamic Assessments

Changes in LV chamber geometry and tissue stiffness invariably occur post-MI[11,17,36,43] and studies have previously shown that the size and mechanical properties of the healing infarct are critical determinants of the LV function post-MI.[15,21] Previous studies regarding scar formation and remodeling in the LV indicated a sizable variability and heterogeneity between specimens, suggesting that the LVFW remodeling following MI could be highly individual.[10] Indeed, unique anatomical and hemodynamic adaptive states were observed in the post-MI subjects of this study, even between subjects at the same timepoint. However, our rodent computational cardiac models account for the individual remodeling states providing a platform that can encapsulate different forms of remodeling, whether, passive, active, or architectural, within a specific subject at a particular timepoint to study their interaction with each other and isolate the contribution of each remodeling event on LV function.

The 1-wk post-MI subjects indicated a slight decrease in the LVFW thickness (Table 2) and a larger LV cavity volume compared to the control (Table 1) accompanied by decreased

LVEF (~22%, Table 1), suggesting that LV eccentric remodeling to maintain normal LV cardiac output may take place as early as 1-wk timepoint. Infarct relative volume measured by DTI was larger in the 2-wk subjects and they exhibited an average ~ 34% decrease in LVEF when compared to control subjects, suggesting a link between the infarct size and loss of function at the 2-wk timepoint. Infarct relative volume and LVEF in 3-wk subjects did not show noticeable differences compared to those of the 2-wk timepoint on average although 3-wk LVFW specimens were stiffer than 2-wk specimens (Figs. 3c and 3d, S4). These observations suggest other remodeling mechanisms can compensate for large increases in infarct stiffness and size and hold off progressive LV decompensation.

Further enlargement and wall thinning of the infarct region was observed in 3- and 4-wk subjects (Fig. S3). Wall thinning in the 4-wk subjects was accompanied by an impaired LVEF compared to the control. The anatomical and hemodynamic characteristics noted in the 4-wk subjects (Table 2) agree with previous studies that chamber dilation and wall thinning dominates over other remodeling events and depresses function in the remote myocardium, leading to reduced organ level output.[27,41]

Predicted Contractile Adaptation of Remote Myocardium

Following an acute MI, the infarcted myocardium loses contractile capacity and it remains unclear whether the remote myocardium undergoes changes in its contractility in order to partially compensate for the impaired LV function. Active contractile forces generated by myocytes can be modulated by changes in the ventricular preload (taken into account in our models through the incorporation of subject-specific geometry and ED pressures) as well as by intrinsic changes in cellular mechanisms and structure (e.g., changes in myofilament protein phosphorylation). The capability to measure contractile forces can provide information as to the adaptive state of the myocardium for improved patient-specific prognosis and therapy evaluation. However, it is not currently feasible to measure contractile forces *in vivo*. Regional cardiac strains are commonly used as alternative measures of myocardial contractility and have been explored as prognostic biomarkers for long-term outcomes in MI. However, tissue-level strains are modulated by several other variables beside myofilament intrinsic contractility including the amount of preload, tissue passive stiffness, and myocardial hypertrophy, rendering regional strains as a confounded metric for adaptations in *fiber-level* intrinsic contractility. Moreover, strains are commonly expressed and analyzed in anatomical coordinates, commonly known as circumferential, radial, and longitudinal (C, R, L) axes. Although these strains are accessible with current imaging technologies and could be appropriate candidates for exploring correlations between global functional metrics and tissue-level motion, they are still confounded measures of the myofiber strain (i.e., regional axial strain in the fiber direction). The myofiber strain, which can better describe microstructural adaptations, can be calculated by transforming strains from (C,R,L) axes into the local architectural axes if the architecture is known.

Our RCCMs predicted an initial increase in the active tension $T_{Ca^{2+}}$ post-MI. The increase was reduced from a nearly fourfold increase in early MI (1-wk timepoint) to a return to near normal values in late-stage MI subjects (3- and 4-wk timepoints). These simulated predictions can be viewed in light of the measurements of LVFW remote thickness,

myofiber orientation in the LVFW (Table 2), and LV cavity dilation. Our numerical results suggested that a thin myocardium in the remote LVFW, a large transmural range of myofiber orientation, and a large LV cavity volume in 1-wk subjects motivated pronounced increases in the $T_{Ca^{2+}}$ in the remote region to preserve a healthy transverse motion. The elevated wall stress brought on by a larger LV cavity as well as a thinner LVFW (based on the Laplace law) in the 1-wk subjects are expected to be key contributors to the necessity of increased contractility to maintain cardiac output. Larger myofiber ranges are considered to impair the transverse contractile motion of the LV, and both the animal-specific models and *in-silico* experiments suggest that higher contractile forces will be required to maintain the cardiac output. The 3-wk MI RCCMs showed a return of $T_{Ca^{2+}}$ to near normal values. Similarly, these results can be viewed in light of the transmural myofiber range. The 3-wk specimens had the largest alignment of fiber orientation towards the circumferential direction which is expected to assist with the improvement of the transverse motion. The 4-wk MI DTI data indicated an alignment of myofibers in the circumferential direction similar to the 3-wk specimens and $T_{Ca^{2+}}$ reduced to a level similar to that of the control subjects. The late-stage MI hearts, however, showed the lowest LVEF values. These observations suggest that decompensated late-stage MI hearts have failed to maintain increased contractility in spite of LV dilation and LVFW thinning. Although thinning and dilation mechanistically increase the regional preload, hence improving the contractility up to a threshold based on the Frank-Starling mechanism, our 4-wk modeling predictions suggest that *progressive* thinning might have led to an extreme reduction in transverse contractility compared to the 1-wk values. In view of these anatomical differences, other remodeling mechanisms, including potential architectural remodeling, are seen to improve the overall contractility of the LV. Interestingly, the proposed adaptive circumferential alignment of myofibers is kinematically driven by seemingly maladaptive anatomical alterations such as LV dilation and wall thinning at least in part.

Estimation of the passive material parameters indicated increased bulk stiffness of the infarct region post-MI, except at the 2-wk timepoint. This result is consistent with the trend seen in the stress-strain curves (Figs. 3c, 3d) and the normalized max stress (Fig. S4). Biaxial data of the 2-wk timepoint was similar to that of the control and the estimated stiffness was found to be similar to that of remote healthy myocardium. This can be partly attributed to the fact that infarct regions were poorly present in some of the 2-wk cohort. While a certain amount of stiffening in the scar region is necessary post-MI to prevent structural failures such as wall rupture, our results suggest that excessive stiffening at later stages of MI, coincident with reduced LVEF, may contribute to a reduction in active tension. One possible mechanism for this is a reduction in preload in an excessively stiff LV chamber, reducing the contractile capacity of the LV through the Frank-Starling mechanism.

Regional Strain: A Composite Index of Contractility in MI

Myocardium regional composition and architecture in the LVFW are designed in the normal heart to produce the optimal contractile pattern resulting in efficient ejection fraction at the organ level upon shortening of individual myofilaments. Remodeling of the fiber organization and collagen fiber content post-MI in the LVFW, as well as changes in the individual myofilament contractility, can independently alter the contractile pattern of

the LVFW and modulate global metrics such as cardiac output. Strain and strain rate measurements are useful *composite* measures of myocardial damage after MI as they are sensitive to a variety of mechanisms altering tissue-level contractility, including fibrosis, myofilament stiffening, and architectural remodeling. Accordingly, the strains have been used as metrics to evaluate myocardial revascularization efficiency and predict patient outcomes with heart failure.[9,12,18] Previous studies have found both longitudinal and circumferential strains post-MI to be independent prognostic indicators of adverse cardiac events post-MI.[23,34,44]

Our simulated strain distributions were consistent with previously reported peak normal strains measured by feature tracking in cardiac magnetic resonance imaging (CMR) and speckle-tracking in echocardiography.[14,31,48,53] Simulated circumferential and longitudinal strains at end-systole were positive in the infarct region at early-stage MI in agreement with *in-vivo* strain studies in a porcine model of MI.[51] Positive, or close-to-zero circumferential and longitudinal strains at end-systole are expected simply due to the lack of active contractility in the infarct zone and increased ventricular pressure during systole inducing distension in passively behaving tissue. The predicted contractile strains in the remote regions of the LVFW were influenced by the non-contractile infarct zone restraining the shortening in the neighboring myocardium. While it may be expected for circumferential and longitudinal strains in the infarct zone to peak at late-stage MI following LV dilation and wall thinning (leading to larger passive tension in the LVFW according to the Laplace law), both strains peaked in the 2-wk timepoint models, likely due to the low infarct stiffness noted at the 2-wk timepoint (Table 2) when compared to the 3- and 4-wk timepoints. The magnitude of the peak strains deteriorated at each subsequent timepoint, coincident with increased infarct stiffness (except at 2-wk), culminating in the lowest contractile strains at 4-wk.

Potential Adaptive Capacity of Fiber Remodeling

The passive biomechanical behavior of the infarct region is dependent on the fiber architecture of the scar tissue that, in turn, is expected to influence the organ-level LV function in MI hearts.[8,13,42] The normal myofiber distribution is organized in such a way that shortening of the fibers results in optimal LVEF; however, the effect of the architecture of the collagen network, which replaces lost myofibers in the infarct region, on the LV function remains to be understood. Also, potential architectural remodeling of the remote myocardium in MI hearts remains understudied. Our subject-specific modeling platform provided an opportunity to investigate these effects *in silico*.

Our *in-silico* experiments predicted that the fiber range in the remote myocardium has an important effect on LV contractility. A synthetically-assigned smaller fiber range at late-stage MI timepoints was found to require lower contractile forces to meet the same LVEF. Alignment of myofibers in the circumferential direction, as seen in our late-stage MI models, was found to partially preserve transverse LVFW motion by reducing the need for increased contractile tension. In contrast, our *in-silico* experiments investigating the effect of infarct fiber architecture on organ-level function predicted only small changes in LVEF, suggesting that the collagen architecture of the infarct region hardly contributes

to global indices. Altered infarct fiber structure did not produce notable changes to EDV, ESV, or LVEF in any subject. Our results suggest that the size and stiffening level of the scar tissue could be more important mechanisms disturbing LV organ-level function that remain to be evaluated. This interpretation of our results is in agreement with a previous parametric study[16] indicating that altered fiber structure, with no change in circumferential-longitudinal stiffness ratio, produces little change in EDV, ESV, or SV. Nevertheless, the fiber architecture of the infarct does impact the LV contractile pattern and function and may influence the end-point of longer-term outcomes.

Multiscale computational models, such as those presented here, are useful tools to offer an improved understanding of interactions between individual remodeling mechanisms enabling the prediction of the optimal state of remodeling in a subject-specific manner. Further studies regarding the impact of infarct fiber structure and properties on long-term LV function could assist with the current development of MI therapies attempting to guide the formation of the infarct architecture by means of mechanical restriction.

Limitations

The results estimated by computational modeling in this study could be quantitatively impacted by approximations in our models. We treated the infarct region as fully transmural and assumed zero contractility, whereas it is possible that the infarct is not fully transmural and maintains some contractile capability. We excluded the presence of an infarct border zone, in which partial contractility may be present. Partial contractility in the infarct and border zone may slightly alter the quantified contractile properties; however, the predicted trend of contractile adaptation is expected to remain similar. In the absence of subject-specific information, mean passive properties were used to model passive myocardial behavior. The estimations of $T_{Ca^{2+}}$ were indeed influenced by the mean stiffening observed across timepoints; however, we did not fully explore interactions between passive stiffness and the estimated active contractility. The estimations of $T_{Ca^{2+}}$ are expected to be quantitatively altered by the variability in the passive parameters indicated by the standard deviations presented in Table 3; however, we expect the overall predicted trend (i.e., increases in $T_{Ca^{2+}}$ in early post-MI and decreases to normal ranges in late post-MI) not to be affected by the variability in passive stiffening in our data. Remote passive properties were assumed not to change in post-MI timepoints requiring further investigation as the majority of existing passive studies of the MI tissues have focused on the remodeling of the scar region. We simplified the model by assuming homogeneous contraction in the remote myocardium and by maintaining the length-dependency parameter, β, constant at all timepoints. Although differences in preload were accounted for as described in “Active Parameter Estimation” section. In the absence of subject-specific infarct architectural data, a layered fiber distribution for the infarct region was used, in which each transmural layer (epicardium, midwall, and endocardium) was assigned a uniform fiber angle. We intend to perform a full comprehensive parametric study on the effect of infarct properties and architecture on LV function in the near future. We attribute the lack of statistical significance between the mean values of hemodynamic measurements across timepoints to the limited cohort of male rats used in this study. Although we have provided evidence of the contractile adaptation post-MI in this cohort, a larger study, involving both male and female

animals, is necessary to fully characterize time-course contractile adaptation. To address these limitations, we are seeking to conduct further studies using a larger cohort of subjects and incorporate 4D cine CMR data[25] to more accurately assess alterations in regional strain and contractility. Additional limitations and the approximations thereof, including the incompressibility assumption for the myocardium,[5,32] the absence of the pericardium[38] and viscoelastic effects in the myocardium,[33,39] and the assumption of identical passive properties for healthy left and right ventricular myocardium,[30] were previously discussed.

Conclusions, Implications, and Future Directions

In this work, we took an essential step towards modeling the concurrent passive and active remodeling of the LVFW following MI. We used rat-specific computational cardiac models of MI to improve our understanding of time-course regional adaptation of the LV post-MI. Ultimately, the delineation of subject-specific LV remodeling, with a focus on regional biomechanical changes throughout the LV, has the potential to examine and complement global functional measures of the LV that provide only limited information on cardiac performance and MI prognosis. We seek to expand our studies of the regional LV remodeling induced by MI and be able to link early-stage strain and contractile measures to long-term outcomes. Results from such studies could improve risk-stratification and early-stage interventions for MI.

Supplementary Material

Refer to Web version on PubMed Central for supplementary material.

ACKNOWLEDGMENTS

This research was supported in part by the National Institutes of Health Grant No. R00HL138288 to R.A.

REFERENCES

1. Arunachalam SP, et al. Regional assessment of in vivo myocardial stiffness using 3D magnetic resonance elastography in a porcine model of myocardial infarction. Magn. Reson. Med. 79:361–369, 2018. 10.1002/mrm.26695. [PubMed: 28382658]
2. Avazmohammadi R, et al. An integrated inverse model-experimental approach to determine soft tissue three-dimensional constitutive parameters: application to post-infarcted myocardium. Biomech. Modeling Mechanobiol. 17:31–53, 2018.
3. Avazmohammadi R, et al. A computational cardiac model for the adaptation to pulmonary arterial hypertension in the rat. Ann. Biomed. Eng. 47:138–153, 2019. 10.1007/s10439-018-02130-y. [PubMed: 30264263]
4. Avazmohammadi R, et al. A contemporary look at biomechanical models of myocardium. Annu. Rev. Biomed. Eng. 21:417–442, 2019. [PubMed: 31167105]
5. Avazmohammadi R, et al. On the in vivo systolic compressibility of left ventricular free wall myocardium in the normal and infarcted heart. J. Biomech. 107:109767, 2020. [PubMed: 32386714]
6. Avazmohammadi R, Hill MR, Simon MA, Zhang W, and Sacks MS. A novel constitutive model for passive right ventricular myocardium: evidence for myofiber–collagen fiber mechanical coupling. Biomech. Modeling Mechanobiol. 16:561–581, 2017.
7. Bachner-Hinenzon N, et al. Strain analysis in the detection of myocardial infarction at the acute and chronic stages. Echocardiography. 33:450–458, 2016. 10.1111/echo.13079. [PubMed: 26412026]

8. Bovendeerd P, Arts T, Huyghe J, van Campen D, and Reneman R. Dependence of local left ventricular wall mechanics on myocardial fiber orientation: a model study. J. Biomech. 25:1129–1140, 1992. 10.1016/0021-9290(92)90069-D. [PubMed: 1400513]

9. Chan J, et al. Differentiation of subendocardial and transmural infarction using two-dimensional strain rate imaging to assess short-axis and long-axis myocardial function. J. Am. Coll. Cardiol. 48:2026–2033, 2006. 10.1016/j.jacc.2006.07.050. [PubMed: 17112992]

10. Chen J, Ceholski DK, Liang L, Fish K, and Hajjar RJ. Variability in coronary artery anatomy affects consistency of cardiac damage after myocardial infarction in mice. Am. J. Physiol. Circ. Physiol. 313:H275–H282, 2017. 10.1152/ajpheart.00127.2017.

11. Collier P, Phelan D, and Klein A. A test in context: myocardial strain measured by speckle-tracking echocardiography. J. Am. Coll. Cardiol. 69:1043–1056, 2017. 10.1016/j.jacc.2016.12.012. [PubMed: 28231932]

12. Dandel M, Lehmkuhl H, Knosalla C, Suramelashvili N, and Hetzer R. Strain and strain rate imaging by echocardiography—basic concepts and clinical applicability. Curr. Cardiol. Rev. 5:133–148, 2009. 10.2174/157340309788166642. [PubMed: 20436854]

13. Eriksson T, Prassl A, Plank G, and Holzapfel G. Influence of myocardial fiber/sheet orientations on left ventricular mechanical contraction. Math. Mech. Solids. 18:592–606, 2013. 10.1177/1081286513485779.

14. Espe EK, et al. Regional dysfunction after myocardial infarction in rats. Circ. Cardiovasc. Imaging. 10:e005997, 2017. 10.1161/CIRCIMAGING.116.005997. [PubMed: 28838960]

15. Feild BJ, Russell RO, Dowling JT, and Rackley CE. Regional left ventricular performance in the year following myocardial infarction. Circulation. 46:679–689, 1972. 10.1161/01.CIR.46.4.679. [PubMed: 5072769]

16. Fomovsky G, Rouillard A, and Holmes J. Regional mechanics determine collagen fiber structure in healing myocardial infarcts. J. Mol. Cell. Cardiol. 52:1083–1090, 2012. [PubMed: 22418281]

17. Gaasch WH, and Zile MR. Left ventricular structural remodeling in health and disease: with special emphasis on volume, mass, and geometry. J. Am. Coll. Cardiol. 58:1733–1740, 2011. 10.1016/j.jacc.2011.07.022. [PubMed: 21996383]

18. Gjesdal O, et al. Noninvasive separation of large, medium, and small myocardial infarcts in survivors of reperfused st-elevation myocardial infarction. Circ. Cardiovasc. Imaging. 1:189–196, 2008. 10.1161/CIRCIMAGING.108.784900. [PubMed: 19808542]

19. Glower D, et al. Linearity of the frank-starling relationship in the intact heart: the concept of preload recruitable stroke work. Circulation. 71:994–1009, 1985. [PubMed: 3986986]

20. Guccione JM, and McCulloch AD. Finite Element Modeling of Ventricular Mechanics. New York: Springer, 1991.

21. Holmes JW, Borg TK, and Covell JW. Structure and mechanics of healing myocardial infarcts. Annu. Rev. Biomed. Eng. 7:223–253, 2005. 10.1146/annurev.bioeng.7.060804.100453. [PubMed: 16004571]

22. Holmes J, Nuñez J, and Covell J. Functional implications of myocardial scar structure. Am. J. Physiol. Hear. Circ. Physiol. 272:H2123–H2130, 1997.

23. Hung C-L, et al. Longitudinal and circumferential strain rate, left ventricular remodeling, and prognosis after myocardial infarction. J. Am. Coll. Cardiol. 56:1812–1822, 2010. 10.1016/j.jacc.2010.06.044. [PubMed: 21087709]

24. Hunter P, McCulloch A, and Ter Keurs H. Modelling the mechanical properties of cardiac muscle. Prog. Biophys. Mol. Biol. 69:289–331, 1998. [PubMed: 9785944]

25. Keshavarzian M et al. An image registration framework to estimate 3d myocardial strains from cine cardiac mri in mice. In: International Conference on Functional Imaging and Modeling of the Heart, Springer, New York, 2021, pp. 273–284.

26. Kupper W, Bleifeld W, Hanrath P, Mathey D, and Effert S. Left ventricular hemodynamics and function in acute myocardial infarction: studies during the acute phase, convalescence and late recovery. Am. J. Cardiol. 40:900–905, 1977. [PubMed: 930837]

27. Lessick J, et al. Regional three-dimensional geometry and function of left ventricles with fibrous aneurysms. A cine-computed tomography study. Circulation. 84:1072–1086, 1991. 10.1161/01.CIR.84.3.1072. [PubMed: 1884440]

28. Li DS, et al. Insights into the passive mechanical behavior of left ventricular myocardium using a robust constitutive model based on full 3d kinematics. J. Mech. Behav. Biomed. Mater. 103:103508, 2020. [PubMed: 32090941]
29. Li DS, et al. How hydrogel inclusions modulate the local mechanical response in early and fully formed post-infarcted myocardium. Acta Biomater. 114:296–306, 2020. [PubMed: 32739434]
30. Liu H, et al. Distribution pattern of left-ventricular myocardial strain analyzed by a cine MRI based deformation registration algorithm in healthy chinese volunteers. Sci. Rep. 28:45314, 2017. 10.1038/srep45314.
31. Liu W et al. Multiscale contrasts between the right and left ventricle biomechanics in healthy adult sheep and translational implications. Front. Bioeng. Biotechnol. 10, 2022.
32. Liu W, et al. Strain-dependent stress relaxation behavior of healthy right ventricular free wall. Acta Biomater. 152:290–299, 2022. [PubMed: 36030049]
33. Liu H, et al. The impact of myocardial compressibility on organ-level simulations of the normal and infarcted heart. Sci. Rep. 11:1–15, 2021. [PubMed: 33414495]
34. Mangion K, et al. Circumferential strain predicts major adverse cardiovascular events following an acute ST-segment–elevation myocardial infarction. Radiology. 290:329–337, 2019. 10.1148/radiol.2018181253. [PubMed: 30457480]
35. McGarvey JR, et al. Temporal changes in infarct material properties: an in-vivo assessment using magnetic resonance imaging and finite element simulations. Ann. Thorac. Surg. 100:582–589, 2015. 10.1016/j.athoracsur.2015.03.015. [PubMed: 26095107]
36. McKay RG, et al. Left ventricular remodeling after myocardial infarction: a corollary to infarct expansion. Circulation. 74:693–702, 1986. 10.1161/01.CIR.74.4.693. [PubMed: 3757183]
37. Mendiola E, et al. Identification of infarct border zone using late gadolinium enhanced MRI in rats. FASEB J. 36:6220, 2022. 10.1096/fasebj.2022.36.S1.R6220.
38. Mendiola EA, Sacks MS, and Avazmohammadi R. Mechanical interaction of the pericardium and cardiac function in the normal and hypertensive rat heart. Front. Physiol. 838, 2022.
39. Neelakantan S, et al. Abstract 14303: structural remodeling in the left ventricular myocardium underlies systolic dysfunction in myocardial infarction. Circulation. 144:A14303–A14303, 2021. 10.1161/circ.144.suppl_1.14303.
40. Neelakantan S et al. Stress relaxation behavior of left ventricular myocardium in mice. FASEB J. 36, 2022.
41. Nicolosi AC, and Spotnitz HM. Quantitative analysis of regional systolic function with left ventricular aneurysm. Circulation. 78:856–862, 1988. 10.1161/01.CIR.78.4.856. [PubMed: 3168193]
42. Omens JH, Miller TR, and Covell JW. Relationship between passive tissue strain and collagen uncoiling during healing of infarcted myocardium. Cardiovasc. Res. 33:351–358, 1997. 10.1016/S0008-6363(96)00206-4. [PubMed: 9074699]
43. Pfeffer MA, and Braunwald E. Ventricular remodeling after myocardial infarction. Experimental observations and clinical implications. Circulation. 81:1161–1172, 1990. 10.1161/01.CIR.81.4.1161. [PubMed: 2138525]
44. Reindl M, et al. Prognostic implications of global longitudinal strain by feature-tracking cardiac magnetic resonance in st-elevation myocardial infarction. Circ. Cardiovasc. Imaging. 12:e009404, 2019. 10.1161/CIRCIMAGING.119.009404. [PubMed: 31679391]
45. Richardson WJ, Clarke SA, Quinn TA, and Holmes JW. Physiological implications of myocardial scar structure. Compr. Physiol. 5:1877–1909, 2018. 10.1002/cphy.c140067.
46. Soepriatna AH, et al. Three-dimensional myocardial strain correlates with murine left ventricular remodelling severity post-infarction. J. R. Soc. Interface. 16:20190570, 2019. 10.1098/rsif.2019.0570. [PubMed: 31744418]
47. Sutton MGSJ, and Sharpe N. Left ventricular remodeling after myocardial infarction. Circulation. 101:2981–2988, 2000. 10.1161/01.CIR.101.25.2981. [PubMed: 10869273]
48. Torres WM, et al. Regional and temporal changes in left ventricular strain and stiffness in a porcine model of myocardial infarction. Am. J. Physiol. Circ. Physiol. 315:H958–H967, 2018.
49. van den Borne S, et al. Myocardial remodeling after infarction: the role of myofibroblasts. Nat. Rev. Cardiol. 7:30–37, 2009. 10.1038/nrcardio.2009.199. [PubMed: 19949426]

50. Verma A, et al. Prognostic implications of left ventricular mass and geometry following myocardial infarction: the valiant (valsartan in acute myocardial infarction) echocardiographic study. Cardiovasc. Imaging. 1:582–591, 2008. 10.1016/j.jcmg.2008.05.012.

51. Wenk JF, et al. A novel method for quantifying the in-vivo mechanical effect of material injected into a myocardial infarction. The Ann. Thorac. Surg. 92:935–941, 2011. 10.1016/j.athoracsur.2011.04.089. [PubMed: 21871280]

52. Xi J, et al. The estimation of patient-specific cardiac diastolic functions from clinical measurements. Med. Image Anal. 17:133–146, 2013. 10.1016/j.media.2012.08.001. [PubMed: 23153619]

53. Yingchoncharoen T, Agarwal S, Popovic ZB, and Marwick TH. Normal ranges of left ventricular strain: a meta-analysis. J. Am. Soc. Echocardiogr. 26:185–191, 2012. 10.1016/j.echo.2012.10.008. [PubMed: 23218891]

54. Zimmerman SD, Karlon WJ, Holmes JW, Omens JH, and Covell JW. Structural and mechanical factors influencing infarct scar collagen organization. Am. J. Physiol. Circ. Physiol. 278:H194–H200, 2000.

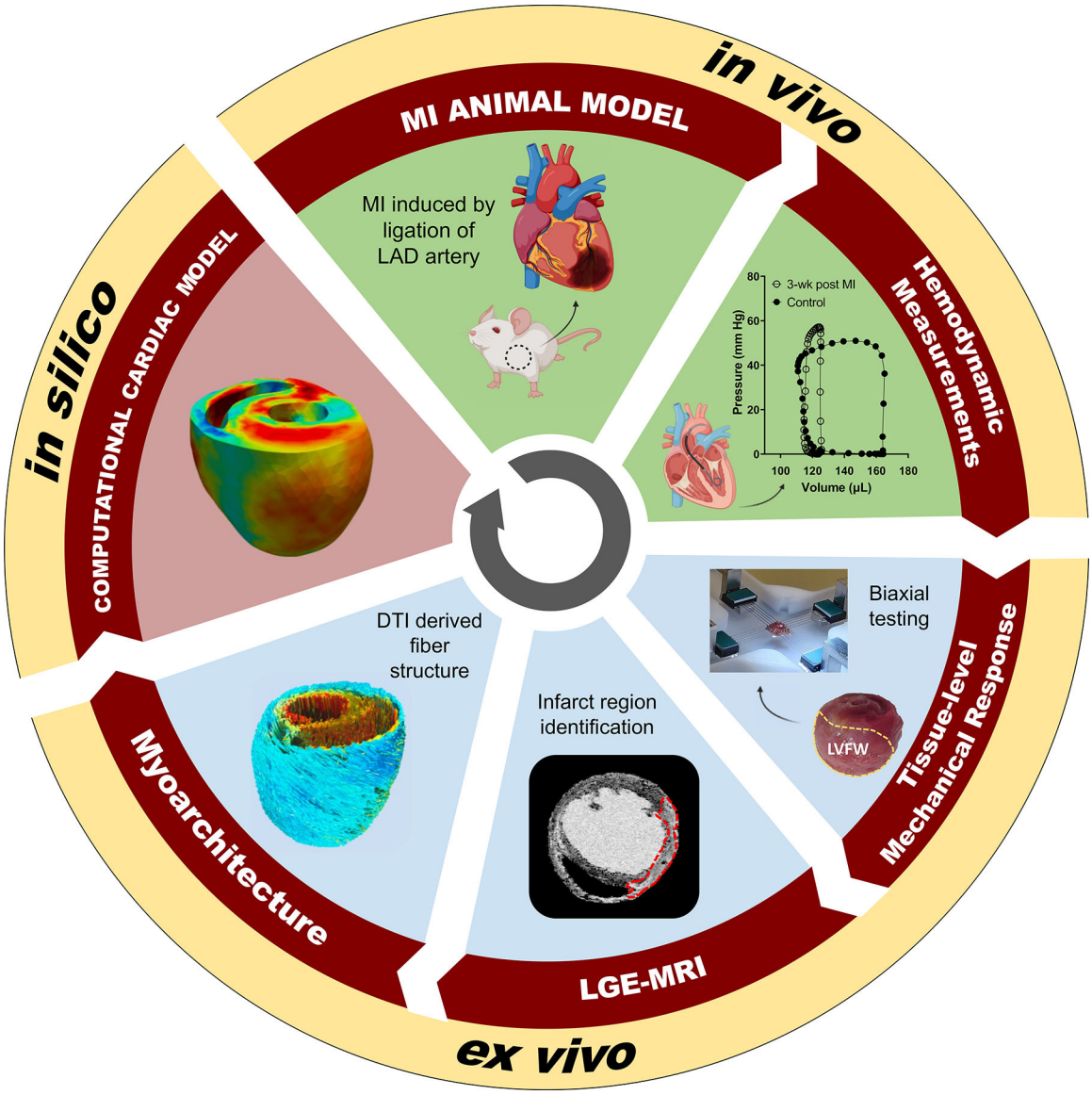

FIGURE 1.

Our modeling pipeline integrated *in-vivo* hemodynamic measurements and *ex-vivo* mechanical and imaging data to develop a high-fidelity subject-specific computational cardiac model. *DTI* diffusion tensor imaging, *LAD* left anterior descending, *LVFW* left ventricle free wall, *MRI* magnetic resonance imaging, *LGE* Late-gadolinium enhancement, *MI* myocardial infarction.

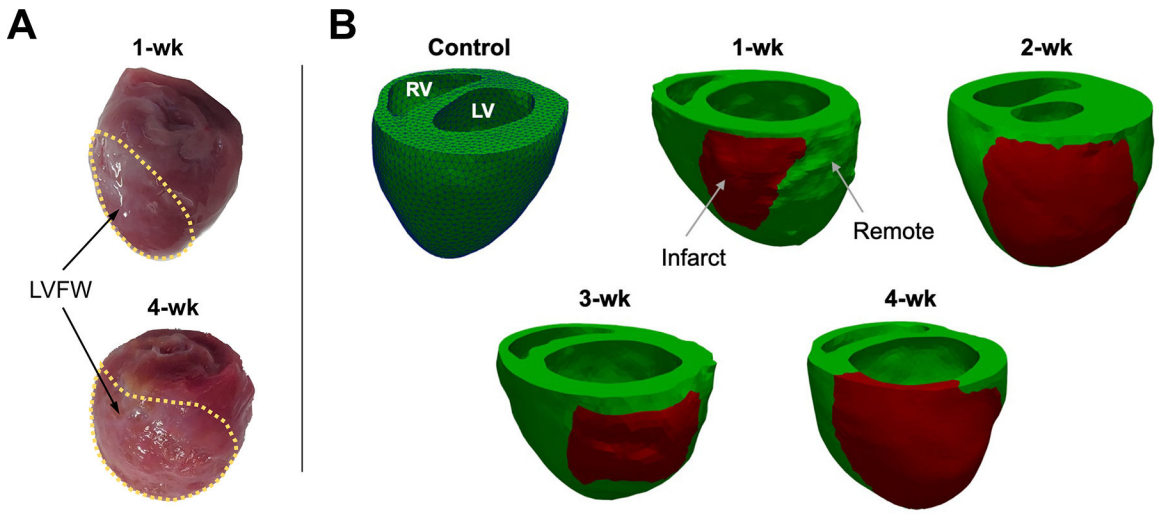

FIGURE 2.

(a) Representative excised hearts and (b) reconstructed biventricular geometries of control heart and post-MI hearts at 1-week intervals post-MI. The green and red regions represent remote and infarct regions, respectively. The control heart is shown with tetrahedral mesh elements visible. *RV* right ventricle, *LVFW* left ventricular free wall, *1-wk* one-week.

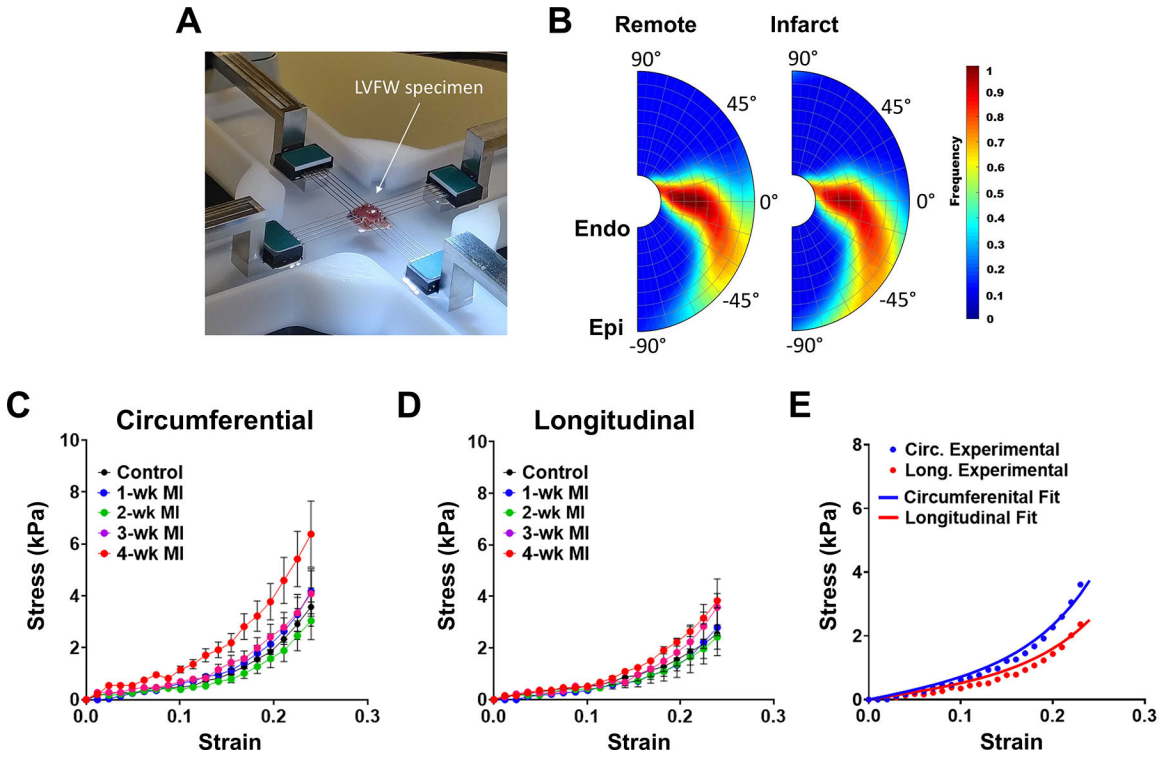

FIGURE 3.

(a) Biaxial mechanical test apparatus. (b) Representative transmural myofiber (left) and collagen (right) helix angle distribution from a 2-wk specimen. (c, d) Mean ± SD of the equibiaxial stress-strain results in the (c) circumferential and (d) longitudinal directions. (e) Representative fit of the mean stress-strain relation from the 1-wk timepoint. Markers and solid lines correspond to experimental data and model fit, respectively.

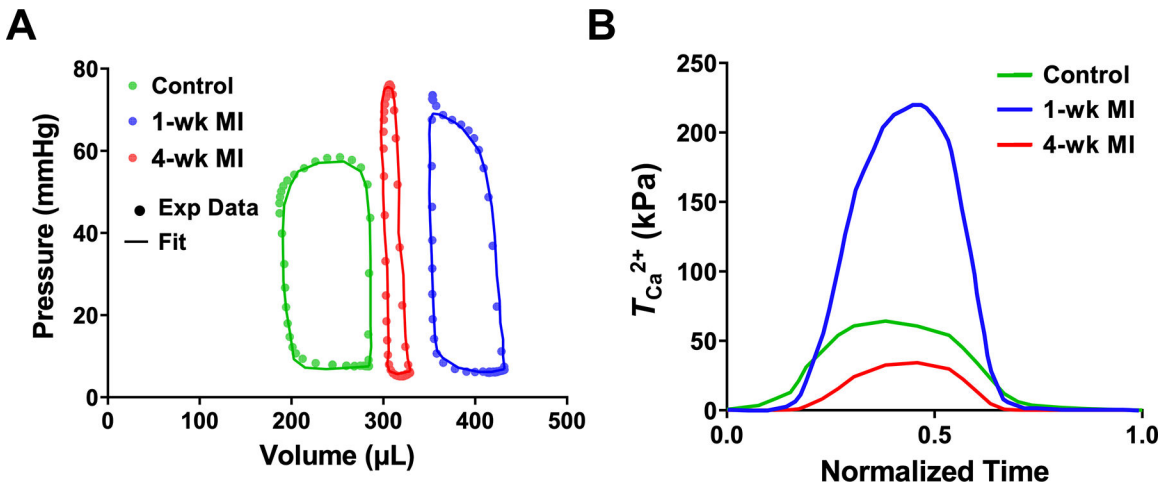

FIGURE 4.

(a) LV pressure-volume loops for the control, 1-wk, and 4-wk hearts (all Subject 1). The markers and lines correspond to experimental data and fitted simulations, respectively. (b) Estimated values of the active parameter $T_{Ca^{2+}}$ over one cardiac cycle for the control (Subject 1), 1-wk (Subject 1), and 4-wk hearts (Subject 2).

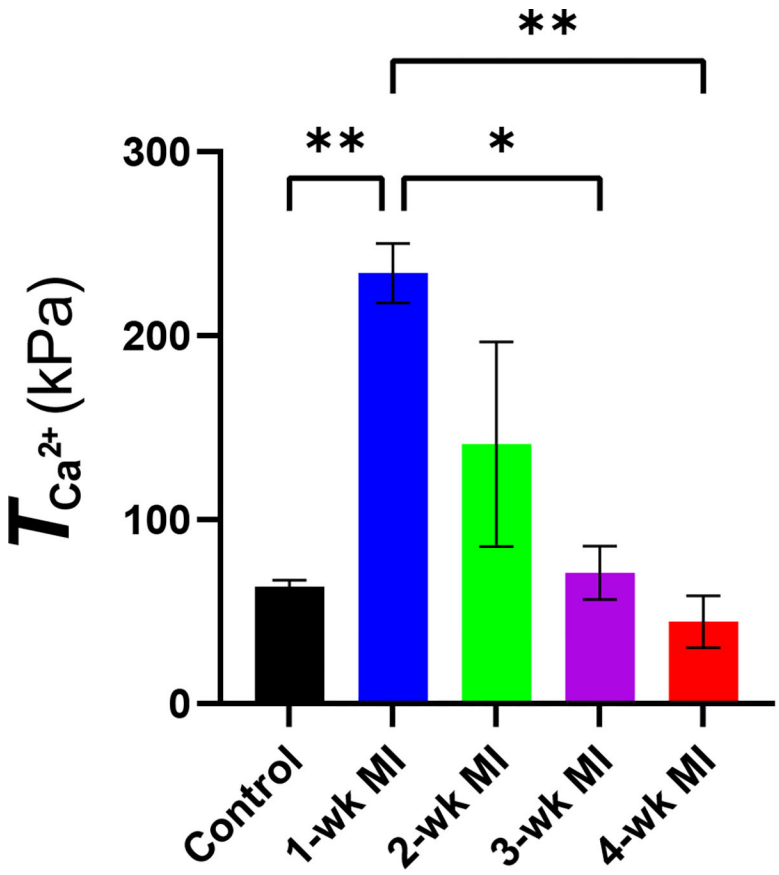

FIGURE 5.

Mean ± SD of the active tension parameter $T_{Ca^{2+}}$ at all timepoints. The statistical significance was calculated by performing ordinary one-way ANOVA with Tukey's multiple comparison test. *$p < 0.05$; **$p < 0.01$. $n = 2$ at each timepoint.

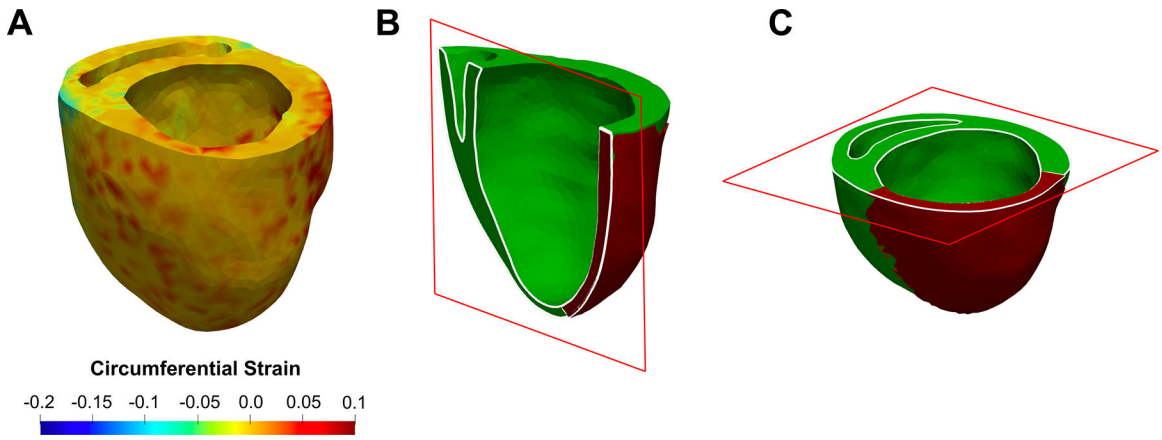

FIGURE 6.

(a) Representative visualization of end-systole strain predictions by FE biventricular model corresponding to a 4-wk heart (Subject 1). Location of (b) long-axis and (c) short-axis slices used in Figs. 7 and 8 for strain visualizations. The long-axis cut was made at approximately the center of the infarct region.

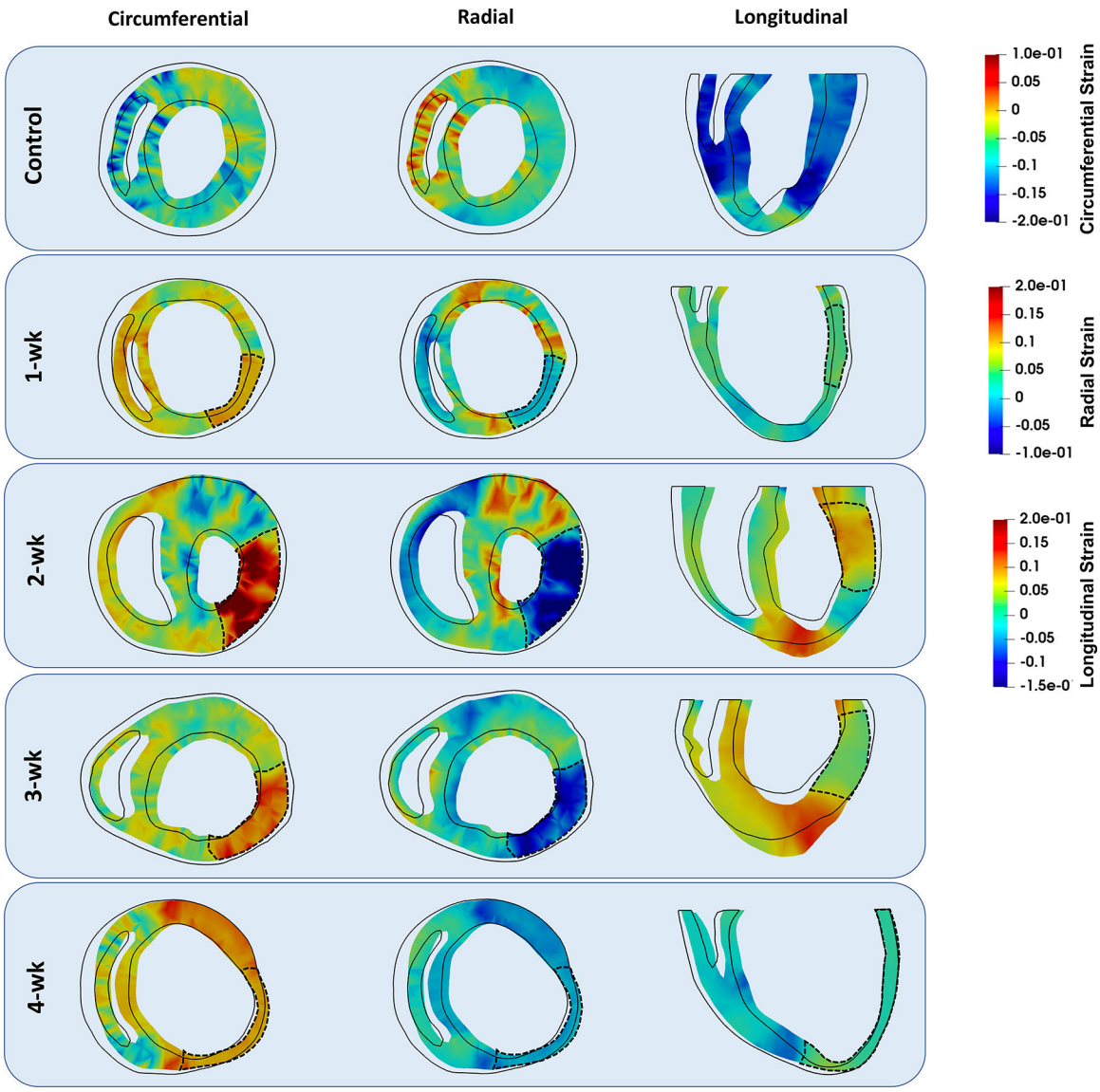

FIGURE 7.

Short-axis and long-axis cross sections of representative rodent computational cardiac models at different timepoints showing circumferential, longitudinal, and radial strains at end-systole. The black outline indicates the geometry of the same cross-section at end-diastole. The dashed line denotes the infarct region in each heart. Data correspond to predictions from Subject 1 models.

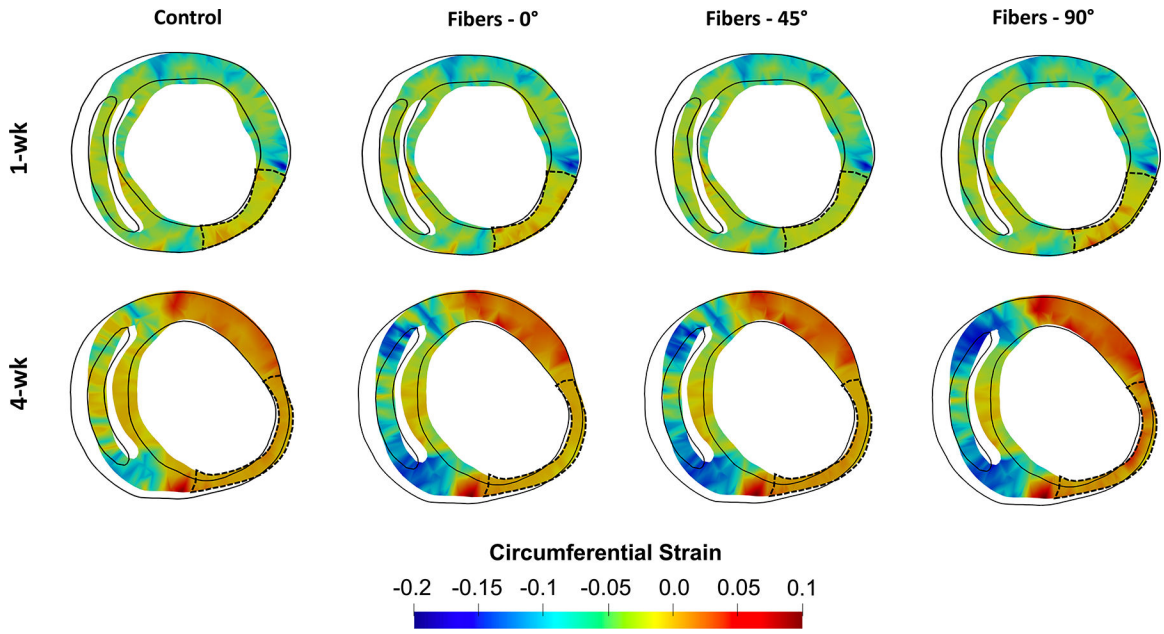

FIGURE 8.

Short-axis and long-axis cross sections of representative 1- and 4-wk (Subject 1) rodent computational cardiac models showing predicted strains resulting from varied fiber structures in the infarct region.

TABLE 1.

Representative echocardiography and catheterization data measured for the control and MI rodents modeled in this study.

	Control		1-wk		2-wk		3-wk		4-wk	
	S1	**S2**	**S1**	**S2**	**S1**	**S2**	**S1**	**S2**	**S1**	**S2**
HR (bpm)	289	277	312	232	290	278	261	263	246	254
EDP (mmHg)	7.9	11.7	8.9	6.6	4.5	5.7	4.6	3.6	5.5	10.7
ESP (mmHg)	53.5	53.3	64.2	72.8	53.6	67.3	84.3	82.0	64.9	88.1
EDV (μL)	280.7	169.4	400.9	432.2	164.1	182.5	209.9	634.3	328.3	480.5
ESV (μL)	187.2	125.4	293.5	347.9	121.6	159.7	148.4	553.7	299.7	396.4
SV (μL)	93.5	44.0	107.4	84.3	42.5	22.8	61.5	80.6	28.6	84.1
CO (μL/min)	27,013	12,188	33,522	19,558	12,326	6342	16,052	21,198	7026	21,361
EF (%)	33.3	26.0	26.8	19.5	25.9	12.5	29.3	12.7	8.7	17.5
d*P*/d*t* min (mmHg/s)	− 2299	− 2383	− 2468	− 4596	− 1638	− 2971	− 5836	− 1708	− 2597	− 3376
d*P*/d*t* max (mmHg/s)	2534	2761	2752	4838	3299	3538	5623	2178	3348	3876
Tau (ms)	45.3	46.2	6.5	10.5	59.3	29.9	28.0	92.3	37.4	33.2
Ea (mmHg/μL)	1.20	1.43	0.94	1.87	2.24	5.17	1.96	4.28	4.13	4.2

S1 and S2 refer to Subject 1 and Subject 2, respectively. Statistical analysis of select parameters is shown in Fig. S2.

HR heart rate, *EDP* end-diastolic pressure, *ESP* end-systolic pressure, *EDV* end-diastolic volume, *ESV* end-systolic volume, *SV* stroke volume, *CO* cardiac output, *EF* ejection fraction, *dP/dt min* minimum rate of rise of left ventricular pressure, *dP/dt max* maximal rate of rise of left ventricular pressure, *Tau* left ventricular relaxation time constant, *Ea* arterial elastance.

TABLE 2.

Geometrical and fiber measurements of the LVFW remote and infarct regions at all timepoints calculated from LGE-MRI and DTI scans.

	Control		1-wk		2-wk		3-wk		4-wk	
	S1	**S2**	**S1**	**S2**	**S1**	**S2**	**S1**	**S2**	**S1**	**S2**
Remote LVFW thickness (mm)	2.29	2.59	1.43	1.61	3.37	4.14	2.39	2.08	1.93	1.11
Infarct LVFW thickness (mm)	–	–	1.21	1.64	3.11	3.60	1.81	0.74	0.93	0.89
Infarct Volume (% LV)	–	–	8.3	10.9	21.5	17.2	24.1	18.2	32.6	17.9
Avg. Myofiber angle in the LVFW (°)	− 3	8	7	3	4	5	− 5	8	− 4	4
Avg. Endocardium myofiber angle (°)	51	48	50	56	38	31	19	23	21	34
Avg. Midwall myofiber angle (°)	− 13	5	4	0	2	4	5	4	9	2
Avg. Epicardium myofiber angle (°)	− 48	− 29	− 39	− 42	− 25	− 19	− 13	− 9	− 24	− 29
Myofiber angle range (°)	99	77	89	98	63	89	32	32	45	63

Fiber architecture data was quantified in the remote region of the LVFW. S1 and S2 refer to Subject 1 and Subject 2, respectively. Statistical analysis of select parameters is shown in Fig. S3.

TABLE 3.

Estimated passive material parameters of the myocardium at each timepoint (n = 6 at each timepoint).

	Control	1-wk	2-wk	3-wk	4-wk
ϕ^r	1.0	0.89	0.94	0.83	0.81
ϕ^i	0	0.11	0.06	0.17	0.19
c^r (kPa)	0.58 ± 0.144	0.58 ± 0.144	0.58 ± 0.144	0.58 ± 0.144	0.58 ± 0.144
B_1^r	43.4 ± 8.1	43.4 ± 8.1	43.4 ± 8.1	43.4 ± 8.1	43.4 ± 8.1
B_2^r	30.7 ± 7.5	30.7 ± 7.5	30.7 ± 7.5	30.7 ± 7.5	30.7 ± 7.5
B_3^r	29.8 ± 4.8	29.8 ± 4.8	29.8 ± 4.8	29.8 ± 4.8	29.8 ± 4.8
$c^r \times a^r$ (kPa)	60.3 ± 12.2	60.3 ± 12.2	60.3 ± 12.2	60.3 ± 12.2	60.3 ± 12.2
c^i (kPa)	0	1.03 ± 0.18	0.54 ± 0.12	1.63 ± 0.32	2.58 ± 0.49
B_1^i	0	58.0 ± 2.8	45.0 ± 4.2	55.5 ± 10.6	80 ± 6.9
B_2^i	0	24.6 ± 4.2	34.0 ± 2.8	31.5 ± 2.1	23.0 ± 1.7
B_3^i	0	30.0 ± 4.2	19.0 ± 1.4	33.0 ± 8.5	17.0 ± 8.7
$c^i \times a^i$ (kPa)	0	113.8 ± 8.2	52.6 ± 13.3	195.0 ± 38.2	310.0 ± 58.3

Control values were used in the entire myocardium in the control rodent computational cardiac models, and in the remote myocardium in the post-MI cardiac models. Values listed for post-MI subjects were applied only in the infarct region of the post-MI cardiac models. Mean remote and infarct region volume fractions (ϕ^r and ϕ^i, respectively) were calculated from histology. $c \times a$ is a measure of bulk stiffness, where a is the sum of the values of B constants according to Eq. (7).[52].

TABLE 4.

Active material parameters predicted by the rodent computational cardiac models at each timepoint. $T_{Ca^{2+}}$ was taken to be zero in the infarct region in post-MI models.

	Peak $T_{Ca^{2+}}$ (kPa)	
	Subject 1	**Subject 2**
Control	66.0	61.1
1-wk	222.6	245.5
2-wk	180.4	101.7
3-wk	60.8	81.3
4-wk	54.5	34.6

S1 and S2 refer to Subject 1 and Subject 2, respectively.

TABLE 5.

Magnitude of peak predicted regional circumferential and longitudinal strains at end-systole of representative rodent computational cardiac models at progressive timepoints.

	Control	1-wk	2-wk	3-wk	4-wk
Remote					
Circumferential	0.183	0.091	0.154	0.088	0.035
Longitudinal	0.167	0.059	0.145	0.101	0.045
Infarct					
Circumferential	–	0.092	0.164	0.068	0.026
Longitudinal	–	0.072	0.133	0.067	0.039

Remote and infarct values were taken from the entire LVFW remote and infarct regions, respectively. Data correspond to predictions from Subject 1 models.

TABLE 6.

Remote region fiber range influence on predicted contractility ($T_{Ca^{2+}}$) in the 3- and 4-wk cardiac models (both from Subject 1).

Week 3		Week 4	
Fiber range (°)	$T_{Ca^{2+}}$	**Fiber range (°)**	$T_{Ca^{2+}}$
100°	95.6	75°	78.2
60°	73.7	45° *	54.5
32° *	60.8	15°	40.3

The rows including (*) represents the original $T_{Ca^{2+}}$ from the model using the subject-specific fiber structure obtained from diffusion-tensor imaging.

TABLE 7.

Effects of synthetic alterations in infarct fiber architecture on left ventricular ejection fraction (LVEF).

	Measured rat-specific LVEF	LVEF-synthetic		
		0°	45°	90°
1-wk	19.5	19.4	19.6	19.5
2-wk	25.9	26.0	25.6	26.6
3-wk	29.3	29.3	28.8	29.1
4-wk	8.7	8.7	8.7	8.5

Rat-specific measurements of LVEF and those corresponding to synthetically altered fiber orientations in the infarct region are reported.